


Article

Application of Hierarchical Nanostructured WO₃ and Fe₂O₃ Composites for Photodegradation of Surfactants in Water Samples

Ewa Biaduń, Sylwia Gajewska, Krzysztof Miecznikowski *  and Beata Krasnodębska-Ostrega *

Faculty of Chemistry, University of Warsaw, Pasteura 1, 02-093 Warsaw, Poland; ebiadun@chem.uw.edu.pl (E.B.); sylwia.gajewska@student.uw.edu.pl (S.G.)

* Correspondence: kmiecz@chem.uw.edu.pl (K.M.); bekras@chem.uw.edu.pl (B.K.-O.);

Tel.: +48-22-552-6340 (K.M.); +48-22-552-6357 (B.K.-O.)

Received: 30 October 2019; Accepted: 5 December 2019; Published: 7 December 2019



Abstract: This study describes the utilization of hierarchical photoactive surface films for the decomposition of surfactants in water samples (with different pH). Photoactive films, containing tungsten (VI) oxide and iron (III) oxide (hematite), were deposited in a systematic and controlled manner using a layer-by-layer method. Physicochemical properties of the photoactive materials were developed and characterized using XRD analysis, Raman spectroscopy, water contact angle, voltammetry, and microscopic (SEM) techniques. The resulting multilayer films showed attractive performances in the photodegradation of the anionic surfactant sodium dodecyl sulfate (SDS) and the nonionic surfactant (1,1,3,3-tetramethylbutyl)phenyl-polyethylene glycol (Triton™ X-144) under solar light irradiation. The efficiency of the surfactants' photodegradation was evaluated with a “test” based on a method, which is extremely sensitive to surfactants' interference, with trace analysis of Pb using anodic stripping voltammetry on mercury electrodes (recovery study). The usefulness of hierarchical photoactive systems in the photodegradation of both surfactants is demonstrated in the presence and absence of the applied bias voltage. The maximum decomposition times were 2–3 h and 30 min, respectively. Furthermore, a properly designed layer system may be proposed, matching the pH of the water sample (depending on the treatment on the sampling side).

Keywords: tungsten trioxide; iron oxide; photocatalysts; stripping voltammetry; solar light decomposition; surfactants

1. Introduction

Some organic compounds with varying degrees of biodegradability used in various industries, as well as in everyday life by consumers, should be removed from wastewater due to their toxicity and their mutagenic and carcinogenic properties [1]. Especially dangerous are the surfactants from the textile, metallurgical, chemical, cosmetic, pharmaceutical, and household product industries. Directly, they are not so dangerous to humans and the environment, but these compounds can reduce the surface tension of water [2–5], allowing insoluble or hardly soluble compounds to be dissolved. Monitoring of the content of such pollutants is certainly required. Moreover, the presence of a high content of surfactants in water interferes with the ability to obtain a reliable analytical result using a variety of techniques. It impairs the stage of nebulization in inductively coupled plasma mass spectrometry (ICP MS) and inductively coupled plasma optical emission spectrometry (ICP OES) measurements (due to surface tension change), while high total organic carbon (TOC) interferes with atomic absorption spectrometers (AAS) detection and ICP ionization (torch clogging). Most of the organic compounds are electroactive, making it virtually impossible to use one of the inexpensive electrochemical methods [6].

Usually, determination of trace elements in water samples does not require any sample pretreatment before graphite furnace atomic absorption spectrometry (GFAAS) or ICP MS analysis. However, surfactants present in high concentrations, especially in wastewater, need previous decomposition (or at least a significant reduction in their levels) [6,7]. Reproducible results can be obtained after complete decomposition of the organic matter or decomposition to a form that does not interact with the analyte.

The photocatalysis process is a useful method for removing resistant organic compounds from water that are difficult to remove by conventional methods, e.g., coagulation, sedimentation, and filtration [8–10]. The application of semiconductors as photocatalysts offers an environmentally friendly way of using solar energy to remove different organic compounds in the presence of various catalysts, such as TiO_2 [1,6,11–16], ZnO [17,18], CdS [19,20], ZnS [21], Fe_2O_3 [22–24], Cu_2O [25], ZrO_2 [26], WO_3 [27,28], V_2O_5 [29], and CdSe [30]. In the case of environmental analytical studies, TiO_2 has favorable semiconductor photocatalytic properties, due to its high photocatalytic activity upon irradiation with UV, high stability in a wide range of pH (modified and non-modified water samples), and low price [11], but its major drawback compared to other semiconductors is its relatively low (only 3–5%) utilization of solar light irradiation. In this context, tungsten trioxide seems to be a good choice for the photodegradation of organic compounds. Tungsten oxide is a semiconductor characterized by a relatively low energy band gap of 2.4–2.8 eV and, importantly, it absorbs a quantum of radiation from the visible range of the solar spectrum (wavelength 480 nm) [31,32]. For this purpose, and also its high stability in acidic conditions and good charge-carrier transport properties, this semiconductor is a very attractive material-purifying complex for environmental water samples [8,33,34]. An intensely studied metal oxide semiconductor for the photodegradation of organic matrices is iron (III) oxide, Fe_2O_3 (hematite), as it is fairly stable in aqueous solutions (except in strongly basic or acid conditions), and also due to its high availability, nontoxicity, and chromatic characteristics. Hematite has a narrow band gap value of 2.1 eV, causing an effective absorption of the solar spectrum when compared to those of TiO_2 and WO_3 [35]. However, a small hole diffusion length of 2 to 4 nm in Fe_2O_3 is seen as an important reason for the lower practical conversion efficiencies, in addition to the slow kinetics of oxygen evolution in water splitting, as reported in the literature. This induces interest in using this material as a photocatalyst, due to its effective operation and low cost; it is also considered an environmentally friendly compound.

In recent years, various research groups have focused on improving the performance of pristine photocatalytic materials by combining both metal oxides to obtain binary heterojunction systems which absorb a large fraction of solar light irradiation and have photoactive properties for water splitting [36–40], as well as aiding the decomposition of various organic compounds [41,42]. The favorable energy band positions of both semiconductors allow the transfer of electrons from the conduction band of Fe_2O_3 to WO_3 and holes from the valence band of WO_3 into Fe_2O_3 , which reduces the recombination of the electron–hole pair and results in an efficient charge separation and better photocatalytic efficiency. Several systems composed of Fe_2O_3 and WO_3 have been proposed with various configuration, including mixed films [43,44], host–guest structure [38,45,46], and nanostructure modified nanowires [47,48]. In the literature, there are a few examples utilizing a $\text{Fe}_2\text{O}_3/\text{WO}_3$ system in photodegradation of organic matter, e.g., methylene blue dyes [49–51], phenol [52,53], rhodamine B [23], and antibacterial activity [54]. The process often had to be accelerated with addition of hydrogen peroxide [23,53]. Senthil et al. showed that photocatalysts composed of $\text{Fe}_2\text{O}_3/\text{WO}_3$ obtained by a simple mixing of both pristine compounds exhibited higher photocatalytic activity towards the decomposition of dye (methylene blue) under solar light irradiation [50]. Moshfegh et al. investigated the optical and surface properties of WO_3 and Fe_2O_3 films with a varying ratio of both metal oxides for the photocatalytic processes [55]. The outcomes exhibited that increasing the content of hematite in the binary system led to a reduction in the optical band-gap and then, a rise in optical constants. Furthermore, Sivula et al. observed that the deposition of Fe_2O_3 onto WO_3 scaffolds allows for an increase in electron charge collection [38]. Recently, we showed that the fabrication of mesoporous

WO₃ admixed with the borotungstic-acid-stabilized hematite is capable of generating anodic current associated with the oxidation of water to oxygen.

The aim of this study is to develop a reagent-free decomposition methodology for simplifying the organic matrix (limitation of interferences) before trace metal analysis in water samples containing large amounts of surfactants. From the advanced environmental analysis point of view, e.g., speciation analysis, it is important not to introduce additional reagents that are usually used for decomposition of surfactants. Furthermore, depending on the complexity of the water samples (e.g., acidic or non-modified samples of water), we are able to design a dedicated hierarchical photoactive system suitable for decomposing surfactants in various environmental samples of different pH. For this purpose, we have developed hierarchical active surface films containing tungsten (VI) oxide and iron (III) oxide (hematite), deposited in a systematic and controlled manner (layer-by-layer), as well as mixtures of both oxides. The arrangements of the films utilized as photocatalytic systems in this study of surfactant photodegradation were labeled as: (1) WO₃/Fe₂O₃BW₁₂/WO₃—W/Fe/W, (2) Fe₂O₃BW₁₂/WO₃/Fe₂O₃BW₁₂—Fe/W/Fe, and (3) admixed WO₃ and Fe₂O₃BW₁₂—m-WFe. The resulting multilayer films show attractive performances towards photodegradation of the anionic surfactant sodium dodecylsulfate (SDS) and the nonionic surfactant (1,1,3,3-tetramethylbutyl)phenyl-polyethylene glycol (Triton™ X-114) following illumination with solar light and in the presence and absence of the applied bias voltage. Herein, we propose an approach that can be viewed as a visible light photodegradation alternative to the well-known (commonly used) concept of the UV digestion method. The efficiency of the photodegradation of surfactants in the presence of the hierarchical films was evaluated by the following testing methods: The water contact angle of surfactant solutions and the recovery study of Pb (content at ppb level) using stripping voltammetry with a mercury electrode as a working electrode (highly sensitive to traces of organic matter in the analyzed sample). The latter approach is sensitive to interference originating from surfactants; therefore, it is a suitable analytical method for evaluating the efficiency of photodegradation of these types of interferents. Application of light in the range of 380–800 nm for decomposition of organic compounds can be the core of cheap photomineralizers—without mercury lamps and expensive quartz glass, as an alternative to the “UV stations” currently used in the treatment of drinking water, and a good starting point for the development of a simple technology for using solar light irradiation to support treatment of water and wastewater directly in the contaminated reservoirs.

2. Results and Discussion

2.1. Morphology and Physicochemical Identity of Photocatalytic Systems

The structure and morphology of the proposed photoactive materials were investigated using X-ray diffraction (XRD) spectroscopy. Figure 1 displays the XRD pattern of all proposed photoactive materials, and the results indicated that the materials had a crystalline structure. In the XRD measurements, a pure and highly crystalline monoclinic WO₃ phase was detected (Figure 1), with no diffraction signals associated with added compounds, showing three distinct diffraction signals in the region $2\theta = 23^\circ$ – 25° corresponding to the (1 1 0), (0 0 2), (0 2 0) lattice planes; these were consistent with the values described in the literature [56–59] (JCPDS 72-0677). Some diffraction signals ascribed to tetragonal SnO₂ were also detected (JCPDS 46-1088). The average crystal size of the WO₃ samples, evaluated by utilizing Scherrer's equation on the main intense signal, was of the order of 50 nm. In the hierarchical systems (W/Fe/W—Figure 1, Fe/W/Fe—Figure 1) and admixed (m-WFe—Figure 1) catalyst films, the XRD pattern demonstrated the main orientation of the WO₃ crystallites appearing at around 25 degrees; otherwise, the lattice planes ((1 0 4), (1 1 0), and (0 1 2)) attributed to hematite were in good agreement with the JCPDS 89-0597 standard cards. This indicated that both compounds could influence the identity of the crystalline phase. Furthermore, the positions of the respective diffraction peaks were practically the same as those typical for the single main components. Bearing in mind that the ionic radii of Fe³⁺ and W⁶⁺ atoms are practically similar, and that they are both six

coordinated in structure, it can be seen that tungsten atoms may insert into the hematite structure and that the replacement of iron by tungsten atoms to form Fe–O–W bonds can occur because of the strong interaction. These results do not confirm the formation of ferric tungstate, but such a situation could not be excluded on the interface between the tungsten oxide and hematite layers.

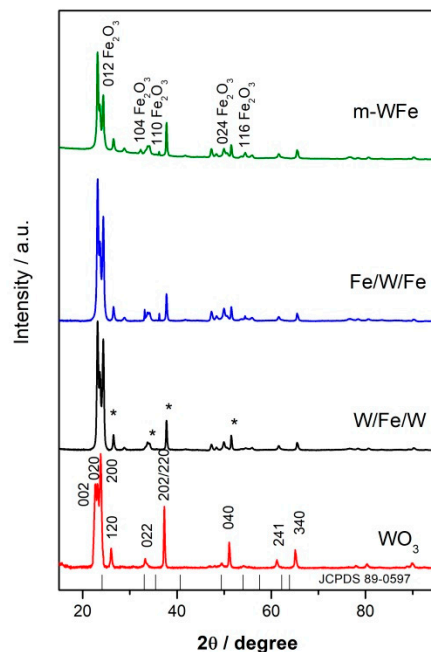


Figure 1. X-ray diffraction pattern of bare WO_3 , mixed m-WFe, and hierarchical systems Fe/W/Fe, W/Fe/W films on the fluorine-doped tin oxide (FTO) conducting glass electrode. Attributes associated with the FTO substrate (SnO_2) are marked by * in the XRD pattern.

The photoactive materials were also analyzed using X-ray fluorescence (XRF), giving the following chemical ratios: The WO_3 samples were pure tungsten trioxide, and the Fe:W atomic ratios for W/Fe/W, Fe/W/Fe, and the admixed m-WFe were 1:100, 10:1, and 1:50, respectively.

To gain insight into the nanostructured morphology of the investigated photoactive material films, scanning electron microscopy (SEM) measurements (Figure 2) were performed on WO_3 , W/Fe/W, Fe/W/Fe, and m-WFe, which were obtained by the layer-by-layer method. Figure 2 shows the surface structure of the pristine WO_3 film before forming the BW_{12} -modified Fe_2O_3 film. It is noteworthy that the pristine photoactive film was composed of grains of WO_3 in a size range of 30–50 nm with porous morphology. More specific changes in morphology were observed in the case of $\text{WO}_3@ \text{Fe}_2\text{O}_3 \text{BW}_{12}$ (Figure 2b), and these were probably related to the presence of three-dimensional structures consisting of Fe_2O_3 and WO_3 crystals of different sizes, typically in the range of 40–80 nm. In the case of the hierarchical system, where bare BW_{12} -modified Fe_2O_3 has formed on top of the WO_3 film (Figure 2c), on the observed surface, small hematite particles with a size of 20 nm can be clearly distinguished from the bigger particles of 30–50 nm, which correspond to monoclinic WO_3 particles. In contrast, in the situation where the pristine WO_3 film was fabricated on the surface of BW_{12} -modified Fe_2O_3 (Figure 2d), no clear hematite grains can be seen; only the typical images of monoclinic WO_3 films are present. This means that the top layer of pristine WO_3 was able to fully cover the intermediate BW_{12} -modified Fe_2O_3 layer.

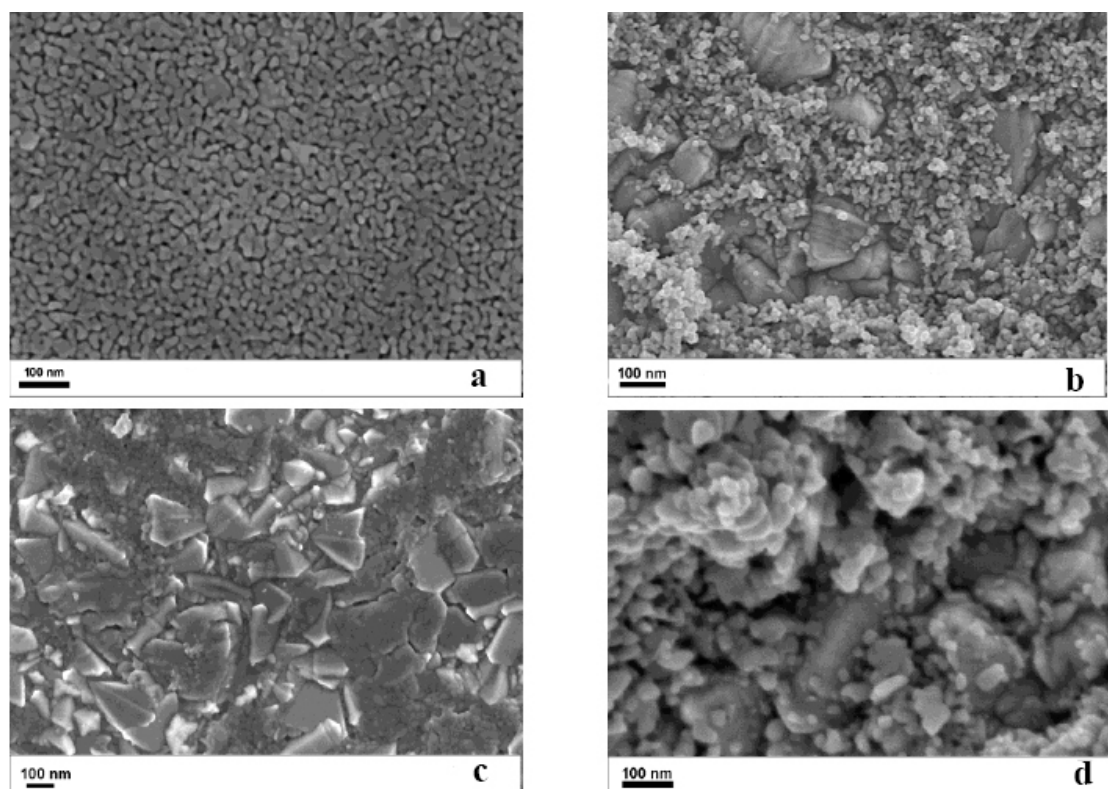


Figure 2. SEM micrographs showing morphology of (a) bare WO₃, (b) admixed m-WFe, and hierarchical systems of (c) Fe/W/Fe, (d) W/Fe/W films.

Additionally, Raman analysis of the proposed photocatalytic materials revealed that the order of the layers was important for the film structure. Significant changes were observed for the intensities of the Raman signals (Figure 3), as well as the appearance of additional peaks concerning the presence of hematite. All of these samples exhibited evidence of two well-defined and strong WO₃ Raman bands at around 715 and 805 cm^{−1}, in addition to two weaker bands around 270 and 325 cm^{−1}, originating from the monoclinic WO₃ structure. These peaks were attributed to the O–W–O stretching and bending modes [56–59], and indicated that peaks from WO₃ nanostructures were present in the spectra of all samples. The noticeable difference between the spectra recorded for the layer-by-layer system and the admixed photoactive materials was related to whether hematite was on top of or inside the films. As observed in Figure 3, all of the films revealed bands around 400 and 1300 cm^{−1} that are mainly attributed to the presence of a certain amount of hematite. Furthermore, when the location of the hematite layer in the photoactive material changed, the intensity of the sharp peaks that originated from hematite at 400 and 1300 cm^{−1} were observed as follows: W/Fe/W (Figure 3a) was less than Fe/W/Fe (Figure 3b) and m-WFe (Figure 3c). In addition, the Raman spectra (Figure 3) did not show the presence of any other iron oxide structure (magnetite or wüstite).

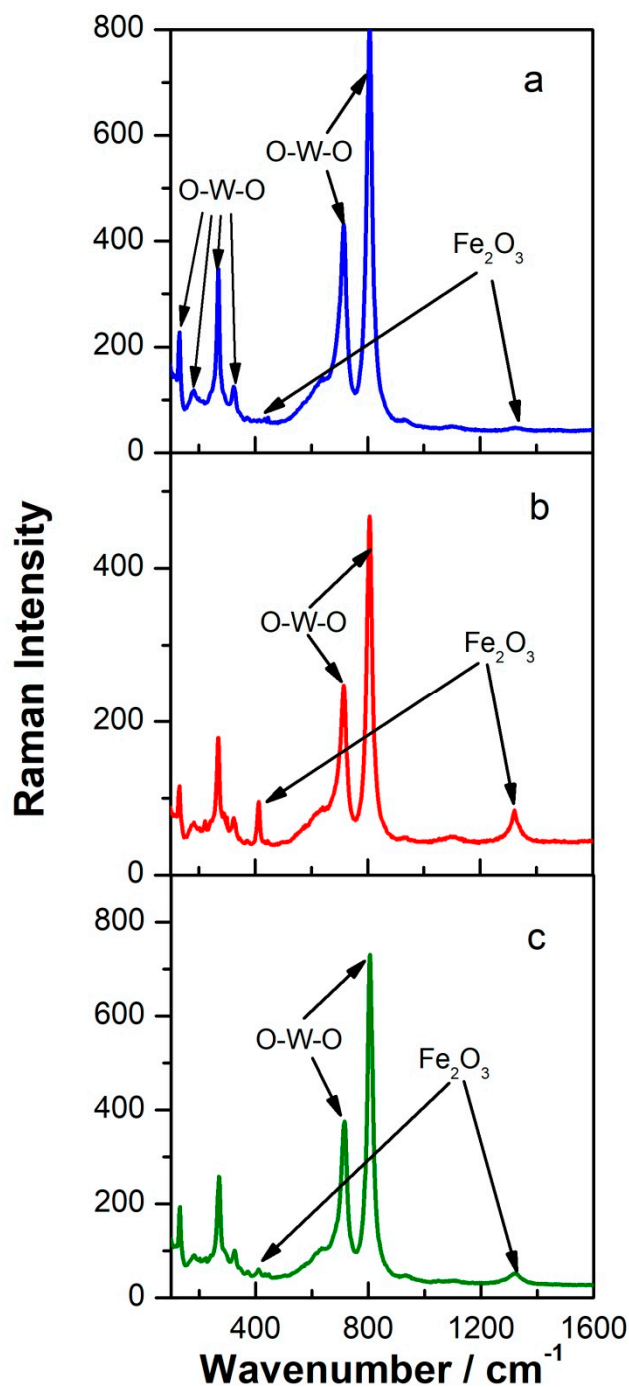


Figure 3. Raman spectra showing changes in the structure of hierarchical systems (a) W/Fe/W, (b) Fe/W/Fe, and (c) admixed m-WFe films on the FTO conducting glass electrode.

The optical absorption spectra of pristine WO_3 and hematite, along with the admixed and layer-by-layer structures, are compared in Figure 4. These samples absorb in the visible range of the solar spectrum. The absorbance of the admixed Fe_2O_3 and WO_3 photoactive material—not only than that of pristine WO_3 and hematite, but also than that of layer-by-layer W/Fe/W—was higher at the longer range of wavelengths. In the case of the Fe/W/Fe system, the observed absorbance signal exceeded that of pristine hematite and the W/Fe/W layer-by-layer structure at all wavelengths.

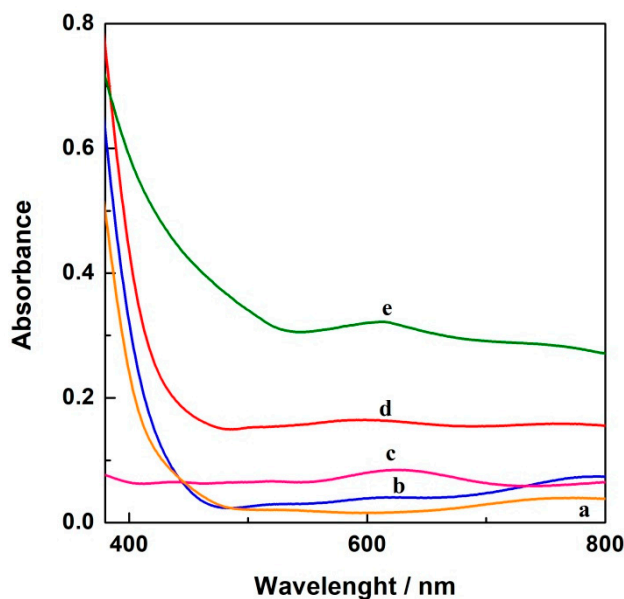


Figure 4. Absorbance spectra of (a) bare WO_3 , (b) W/Fe/W , (c) $\text{Fe}_2\text{O}_3\text{BW}_{12}$, (d) admixed m-WFe , and (e) Fe/W/Fe films on the FTO conducting glass electrode.

The photoelectrochemical performances of the hierarchical tungsten oxide and hematite photoactive materials were also determined. Figure 5 illustrates linear sweep voltammetry (the photocurrent density as a function of the applied potential (E) upon sweeping the potential from 400 to 1400 mV vs. reversible hydrogen electrode (RHE)) under chopped simulated solar AM 1.5 G (100 mW cm^{-2} , spectrally corrected) illumination for each sample in $0.5 \text{ mol dm}^{-3} \text{ H}_2\text{SO}_4$. The conditions of this experiment led to the determination of the onset potential, the maximum photocurrent generated while applying bias to the electrodes, giving insight into the surface recombination events. The control anodic photocurrent density for all samples increased with the growing of the applied voltage. In the case of bare hematite and WO_3 , the onset potentials of the photocatalytic processes were determined by examination of the recorded photocurrent during illumination, which was continually switched on and off. The values determined were 0.56 and 0.60 V, respectively, for WO_3 and hematite. The observed onset potential was only slightly negatively shifted for WO_3 in comparison with hematite. The maximum photocurrent density values at 1.2 V were 1.1 and 1.0 mA for pristine WO_3 and Fe_2O_3 , respectively. Compared to the hierarchical photoactive materials containing WO_3 and Fe_2O_3 , as well as admixed oxides, the hierarchical system with WO_3 on top and an admixed composition caused a negative shift of the onset potential for the anodic process of ca. 80 mV. On the other hand, the hierarchical system with hematite located on top caused a positive shift of the onset potential for the anodic process of ca. 40 mV. The maximum photocurrent density values of the photoactive films, W/Fe/W , Fe/W/Fe , and m-WFe , were much more similar because they showed saturation current densities (at 1.2 V) equal to 1.6, 1.7, and 1.5 mA, respectively.

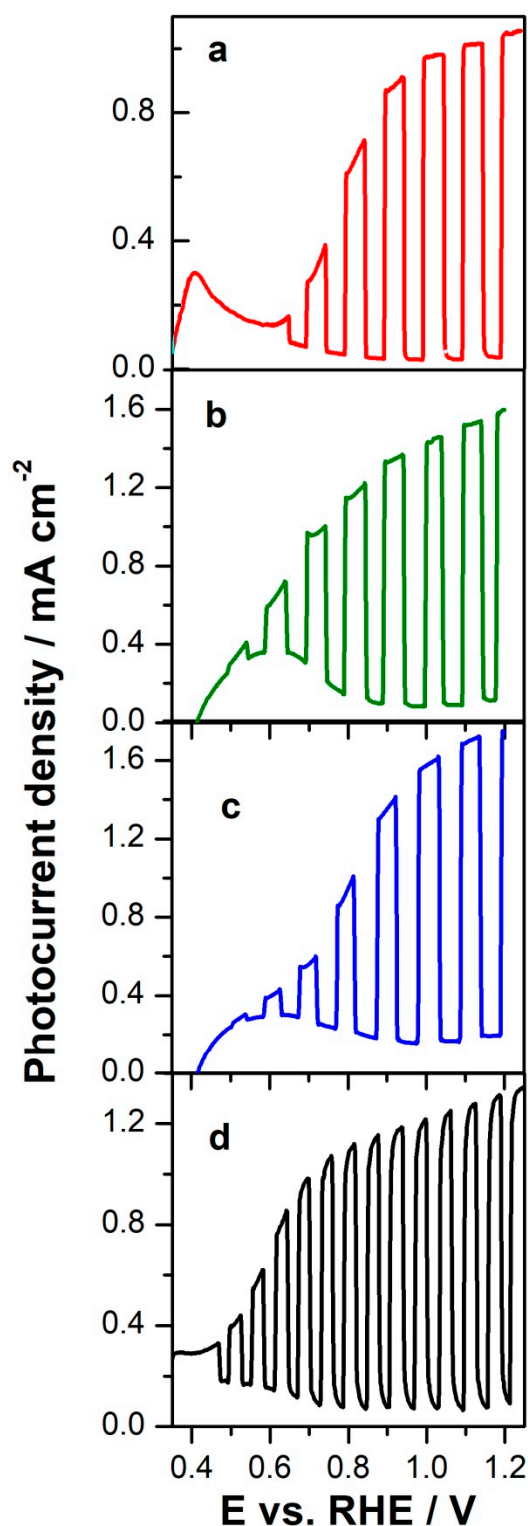


Figure 5. Photocurrent recorded as a function of the electrode potential under chopped simulated solar AM 1.5 G illumination of (a) bare WO₃, (b) W/Fe/W, (c) Fe/W/Fe, and (d) admixed m-WFe, films on the FTO conducting glass electrode. Electrolyte: 0.5 mol dm⁻³ H₂SO₄. Scan rate: 10 mV s⁻¹.

The enhanced performance of photoelectrodes composed of various linkages of WO₃ and hematite could be attributed to the lower position of the conducting band of hematite in comparison to that of WO₃. Moreover, in this condition, it could not be excluded that the decreasing recombination rates of electron–hole pairs enhanced the photo-generated electron transfers.

2.2. Decomposition of SDS and TritonTM X-114

It is commonly known that the surfactants present in solutions during voltammetry measurements change the electrochemical processes occurring on the surface of the electrode, significantly reduce the surface tension of mercury, and could additionally be adsorbed at the electrode surface by their hydrophobic tails and form a hydrophobic layer at the surface of the electrode [60].

2.2.1. Photodegradation without Application of Potential Difference

Sodium dodecylsulfate interferes with the recorded signal of Pb mostly by forming an electroactive complex (Pb-SDS) which is adsorbed on the electrode. Therefore, the Pb oxidation peak was utilized to indicate the efficiency of the surfactants' photodegradation. In the case of SDS, voltammetric measurement was carried out on the samples taken after 2, 3, and 4 h of irradiation. A total of 20 ng of Pb was added to the voltammetric cell. The recovery of Pb was a measure of the degree of the surfactants' decomposition. As a rule, the recovery range of Pb was calculated based on four to six experimental measurements (two to three replications for each of two plates for each composition of the active layer), the correlation coefficient (R^2), and the mean value of the slope of the line. The results obtained are shown in Table 1. After 2 h of irradiation, the resulting voltammograms had a typical voltammetric Gaussian shape, with a well-defined analytical signal associated with lead oxidation (Figure 6). The lead oxidation peak was recorded at -0.420 V. The analytical signal for lead oxidation increased after subsequent additions of standard solution. Longer mineralization time did not cause a shift in the peak potential of lead oxidation, which was constant and did not depend on the irradiation time or the additions of standard solution of lead. At higher potential values, the appearance of additional signals due to the generation of an electroactive complex of SDS and lead can be expected (Figure 6). In the case of the admixed m-WFe photoactive system, the range of recoveries obtained for samples after 3 h of irradiation was practically the same as that obtained after 4 h of irradiation. The recovery range obtained after different digestion times overlapped. A similar trend was observed when the W/Fe/W photoactive material was utilized. A different situation was observed when the Fe/W/Fe photoactive system was utilized; with increasing irradiation time, higher recovery values were obtained. In this case, the best efficiency of surfactant digestion was obtained after 4 h of irradiation time (Table 1). The lowest dispersion of recovery values was obtained in the presence of the Fe/W/Fe active layer after 4 h of irradiation (7%). It is important to note that, for Fe/W/Fe samples, photodegradation of the surfactants was performed at a higher pH (pH = 5) in comparison to previous samples. The results are promising in the context of speciation analysis [61]. In each sample, the coefficient of correlation was close to 100%, and the relative standard deviation of the triple measurements did not exceed 1%, which was fully predictable. The calibration curve based on the height of electrochemical signals as a function of the concentration of lead showed a linear dependence within the full range of investigated Pb concentration, with slopes of 0.047, 0.015, 0.042, and 0.036, respectively. The results regarding the slopes provided good evidence of the sensitivity of the method, and the best sensitivity in the process of photodegradation of SDS was shown by the Fe/W/Fe system.

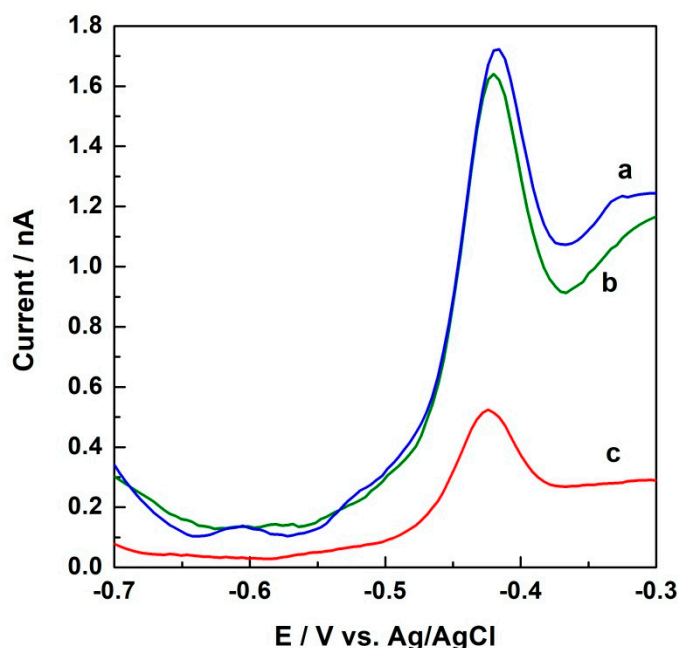


Figure 6. Differential pulse anodic stripping curves of the water sample recorded using HMDE in the solution containing 20 ng of Pb and 1.67×10^{-4} mol L⁻¹ of sodium dodecylsulfate (SDS) after decomposition in the presence of (a) Fe/W/Fe (pH = 5), (b) m-WFe (pH = 2), and (c) W/Fe/W (pH = 2) assisted with solar light irradiation over 3 h after 75 s of deposition at −0.9 V.

In the next experiment, the model anionic surfactant SDS was replaced by the nonionic surfactant TritonTM X-114. Generally, the nonionic surfactants are significantly more resistant to photodegradation than other groups of surfactants, and they significantly reduce surface tension. In this case, a reproducible voltammetric signal was recorded in a potential range from −0.420 to −0.430 V. The peaks obtained after the second and third addition of Pb standard solution completely overlapped with the peak recorded after addition of the first portion of the 20 ng of Pb. With all of the studied photoactive materials utilized for the photodegradation of Triton after 2 h of irradiation by solar light, the signal originating from the interferent was not observed, whereas longer irradiation time allowed us to obtain a higher recovery of Pb (Table 1). In the case of the hierarchical Fe/W/Fe photoactive materials, increasing the irradiation time to 4 h gave higher recovery values, while increasing the irradiation time to 6 h did not cause any further increase. The average recovery values reached 85%, 90%, and 91% for 2, 4, and 6 h, respectively. The application of W/Fe/W with Triton made it possible to obtain an approximately 100% recovery of Pb after 2 h of irradiation with solar light. For the admixed m-WFe photoactive system, it can be clearly seen from Table 1 that the recovery value of Pb after 2 h of irradiation was slightly lower in comparison to that of the W/Fe/W photoactive system. When the irradiation time was increased to 4 h, the recovery of Pb was practically the same as for the W/Fe/W system, and further increasing of the irradiation time did not lead to a higher recovery of Pb. Extension of the irradiation time for an additional 2 h in the presence of admixed m-WFe photoactive material led to an improvement in the photodegradation efficiency of TritonTM X-114 and in the sensitivity of the method.

Table 1. Recovery of 20 ng of Pb in the presence of SDS and Triton™ X-114 before and after illumination of the samples in the presence of various active layers. Sample volume: 46 mL.

Active Layer	Irradiation Time [h]	Recovery [%]	R ² [%]	Slope
SDS				
no irradiation		80.4–86.1	99.62	0.0179
m-WFe	2	98.0–127.5	99.54	0.0148
	3	94.5–136.6	99.81	0.0529
	4	99.1–124.9	99.84	0.0163
Fe/W/Fe	2	92.8–108.0	99.99	0.0423
	3	86.4–98.8	99.98	0.0451
	4	99.4–106.1	99.98	0.0453
W/Fe/W	2	70.9–91.7	99.75	0.0358
	3	85.9–103.3	99.02	0.0436
	4	93.1–106.0	99.99	0.0375
Triton™ X-114				
no irradiation		75.3–86.3	99.95	0.0429
m-WFe	2	82.4–91.5	100.00	0.0465
	4	96.5–104.1	100.00	0.0426
	6	98.5–119.6	99.06	0.0417
Fe/W/Fe	2	84.5–85.1	99.99	0.0393
	4	88.5–91.5	99.99	0.0455
	6	90.1–91.3	100.00	0.0410
W/Fe/W	2	97.0–106.2	100.00	0.0439
	4	97.9–100.0	99.90	0.0398
	6	98.8–105.8	100.00	0.0408

This work has also been expanded to determine the influence of the sample volume on the photodegradation efficiency of Triton™ X-114. Additional photoelectrochemical diagnostic experiments were performed in smaller sample volumes, but with the same concentration of the surfactant. For this purpose, samples containing 23 mL of 11 $\mu\text{g mL}^{-1}$ of Triton™ X-114 were irradiated for 4 h, and these samples were analyzed after 2, 3, and 4 h of irradiation with solar light. Depending on the nature of the applied photoactive materials, the solution was adjusted to pH = 2 using nitric acid. It is important to note that, for all of the utilized photoactive materials, no signal originating from interference was recorded, and the signals from the addition of standard solutions of Pb were repeatable; peak positions and shapes were not affected. The results obtained after 2, 3, and 4 h of irradiation are presented in Table 2. The highest recovery values were obtained after 4 h of photodegradation for the admixed active layers m-WFe. The two remaining photoactive systems showed slightly lower values of recovery in comparison to that of the admixed photoactive layer of tungsten oxide and hematite, m-WFe. Moreover, the ranges of recovery obtained after 3 h of illumination with solar light, for both W/Fe/W and the admixed m-WFe photoactive systems, overlapped with the ranges of recovery found after 4 h under simulated solar light irradiation. Hence, prolongation of the illumination time to more than 3 h did not influence the efficiency of photodegradation of Triton™ X-114. In other words, after just a 3 h period of mineralization, recovery results similar to those of after 4 h were obtained.

Table 2. Recovery of 20 ng of Pb in the presence of TritonTM X-114 after illumination of the samples in the presence of various active layers. Sample volume: 23 mL.

Active Layer	Irradiation Time [h]	Recovery [%]	R ² [%]	Slope
m-WFe	2	95.7–96.8	99.99	0.052
	3	95.7–101.8	99.92	0.049
	4	97.5–100.7	99.68	0.051
Fe/W/Fe	2	89.8–91.5	99.93	0.051
	3	89.7–92.2	99.97	0.048
	4	96.2–98.1	99.96	0.051
W/Fe/W	2	91.2–94.1	99.97	0.048
	3	92.9–99.4	99.85	0.052
	4	96.6–97.9	99.78	0.054

2.2.2. Influence of Bias Voltage on the Photodegradation of Surfactants

The influence of applied bias on the photodegradation of surfactants on the prepared photoactive materials was studied. The presence of an electrical field (photoelectrocatalytic process) reduces the electron–hole recombination, improving quantum efficiencies and thus the photoelectrocatalytic activity of the hierarchical layers towards the decomposition of surfactants. The results obtained for the admixed active layers m-WFe are displayed in Figure 7. A well-defined peak for lead oxidation appeared at a potential of around -0.43 V. The recovery rates for sample mineralization in runs with Pb and TritonTM X-114 are summarized in Table 3, confirming the enhanced effect of parallel irradiation treatment and applied bias in the presence of the examined hierarchical photoactive materials on the amount of detectable Pb (II) and the efficiency of decomposition of organic species in the samples. After 0.5 h of photoelectrochemical degradation of samples containing TritonTM X-114, the highest recovery of lead (around 99%) was obtained in the presence of the Fe/W/Fe photoactive system. Prolongation of the illumination time for an additional 0.5 h caused the increase of Pb recovery to 100%. When the W/Fe/W photoactive system was utilized for photoelectrochemical degradation of TritonTM X-114, the recovery of lead approached 90% after 0.5 h of illumination with solar light. In order to achieve a 100% recovery of lead, the illumination time had to be extended for an additional 0.5 h, or even slightly more, up to 1.5 h in total (Table 3). The admixed tungsten oxide and hematite m-WFe photoactive system showed around 94% recovery of lead occurring within 0.5 h of illumination with solar light. In this case, even after 2 h of irradiation with applied bias, the recovery of lead did not reach 100%. The better photoelectrochemical degradation capacity of the photoactive material with hematite as its outer layer in comparison with the other two photocatalysts examined here may be due to the combined effects of its well-developed surface area and heterojunction nanostructure.

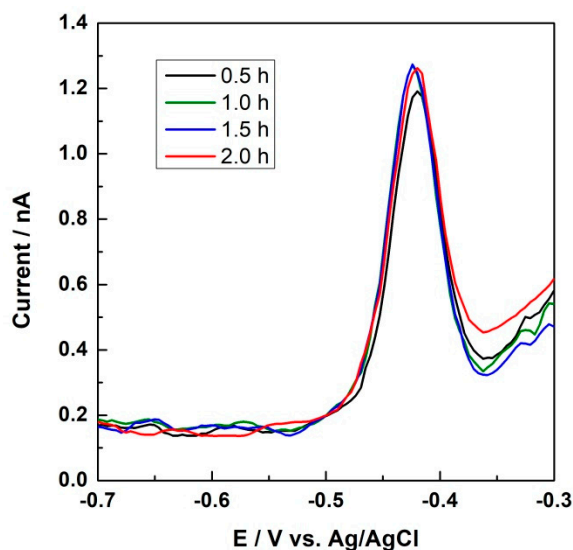


Figure 7. Differential pulse anodic stripping curves of the water sample recorded using the hanging mercury drop electrode (HMDE) in the solution containing 20 ng of Pb and $1.97 \times 10^{-5} \text{ mol L}^{-1}$ of Triton™ X-114 after decomposition in the presence of m-WFe (pH = 2) assisted with solar light irradiation with applied bias voltage (1.2 V) over 0.5, 1, 1.5, and 2 h; deposition time: 75 s at -0.9 V .

Table 3. Recovery of 20 ng of Pb in the presence of Triton™ X-114 after different illumination times with applied bias voltage (1.2 V) and in the presence of three various active layers.

Active Layer	Irradiation Time [h]	Recovery [%]	R ² [%]	Slope
m-WFe	0.5	92.8–94.1	99.99	0.049
	1	90.6–93.6	99.60	0.050
	1.5	93.0–95.1	99.98	0.051
	2	95.8–97.3	99.88	0.049
Fe/W/Fe	0.5	97.7–99.1	99.88	0.038
	1	99.2–101.3	100.00	0.045
	1.5	102.1–103.8	99.95	0.049
	2	104.7–107.4	98.45	0.047
W/Fe/W	0.5	85.4–87.9	99.98	0.062
	1	92.7–98.2	99.94	0.048
	1.5	100.9–106.5	100.00	0.055
	2	100.3–109.1	100.00	0.050

To confirm the results of photodecomposition of surfactants described above, additional water contact angle measurements were performed for the samples containing Triton™ X-114 before and after illumination with solar light, both with and without an application of potential. The data in Figure 8 shows representative pictures of water droplets relating to the illumination time, both with and without an applied bias. The water contact angle values for the samples containing Triton™ X-114 after 0, 2, 4, and 6 h of illumination in the presence of the W/Fe/W photocatalyst were found to be equal to 84° , 80° , 75° , and 70° , respectively (Figure 8A). For comparison, the water contact angle measurements were also performed for the samples containing Triton™ X-114 after illumination in the presence of the W/Fe/W photocatalyst upon application of the potential. The values determined were 78° , 72° , and 66° for 0.5 h, 1 h, and 2 h, respectively. In both cases, the gradual decrease of the water contact angle with the illumination time that was recorded for W/Fe/W both with and without

an applied bias voltage may result from the photodecomposition of surfactants present in the water sample. This result is in good agreement with the measurements of Pb recovery.

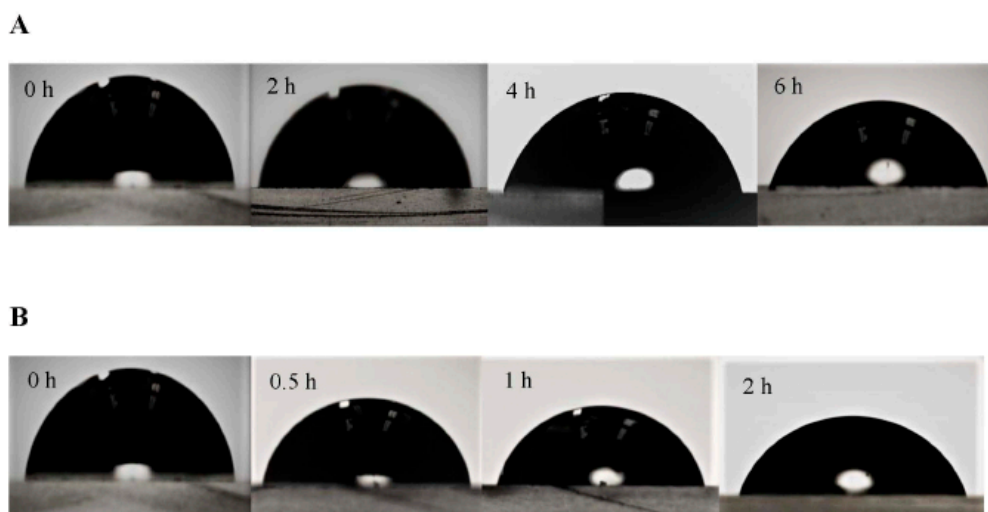


Figure 8. The contact angle of a water sample containing Triton™ X-114 as a function of irradiation time with solar light in the presence of hierarchical photoactive films (W/Fe/W) without (A) and with (B) applied bias voltage.

2.2.3. Spectrophotometric Analysis

In the context of elemental analysis, total decomposition of surfactants is not required; simplification of the organic matrix is sufficient enough to minimize their interference. The UV-Vis measurements were used to monitor the characteristic signals for the studied surfactants during the photodegradation process. Figure 9a displays the UV-Vis spectra of Triton™ X-114 after photodegradation over m-WFe, W/Fe/W, and Fe/W/Fe photocatalysts under different illumination times with solar light, with and without bias potential. The photodegradation of Triton X-114 was monitored during this time by its UV-Vis spectrum by following the changes to the two characteristic maximum absorbance bands for Triton™ X-114 at 230 and 250 nm. The latter absorbance band originates from the π - π transition relating to the presence of an aromatic system. Both maximum absorbance bands of Triton™ X-114 gradually decreased, but there was no shift in the bands' positions during the photodegradation process in the presence of any of the investigated systems. These results indicated that the photodegradation of Triton™ X-114 had already occurred within 2 h in the presence of two of the photoactive systems (W/Fe/W and m-WFe; Figure 9b). Furthermore, the same experiments were performed with applied bias potential (Figure 9c), which provides another driving force for the accelerated oxidation of surfactants at the surface of the photoactive materials. What is interesting is that the characteristic absorbance band of Triton™ X-114 decreased totally during its photoelectrochemical degradation after 0.5 h of solar light illumination in the presence of the hierarchical W/Fe/W and Fe/W/Fe photoactive layers. In other words, the application of potential to the photoactive layers allows for the irradiation time to be significantly reduced in the presence of hierarchical photoactive materials composed of tungsten oxide and hematite. It is noteworthy that the proposed hierarchical photoactive system exhibited higher photodegradation efficiency and lower decomposition time (after 30 min under a bias voltage) in comparison with that of the other reported systems [62–64]. For instance, the mineralization rate of Triton™ X-114 reached up to 26% using TiO₂ under UV irradiation after 120 min, but with an additional oxidizing reagent (hydrogen peroxide), the degradation rate achieved 67% after 120 min [63]. High efficiency of photodegradation of some organic compounds in water [23,53] could be reached after some addition of an oxidizing reagent. However, the proposed layers work in reagent-free options. Furthermore, Barreca et al. [52] showed the high potential of applicability of high-purity WO₃ dispersion on Fe₂O₃ deposit systems

prepared by a two-step vapor phase process in photodegradation of organic compounds (e.g., phenol) in water. They also show the high usefulness of this type of hierarchical photoactive system for the photodegradation of organic compounds.

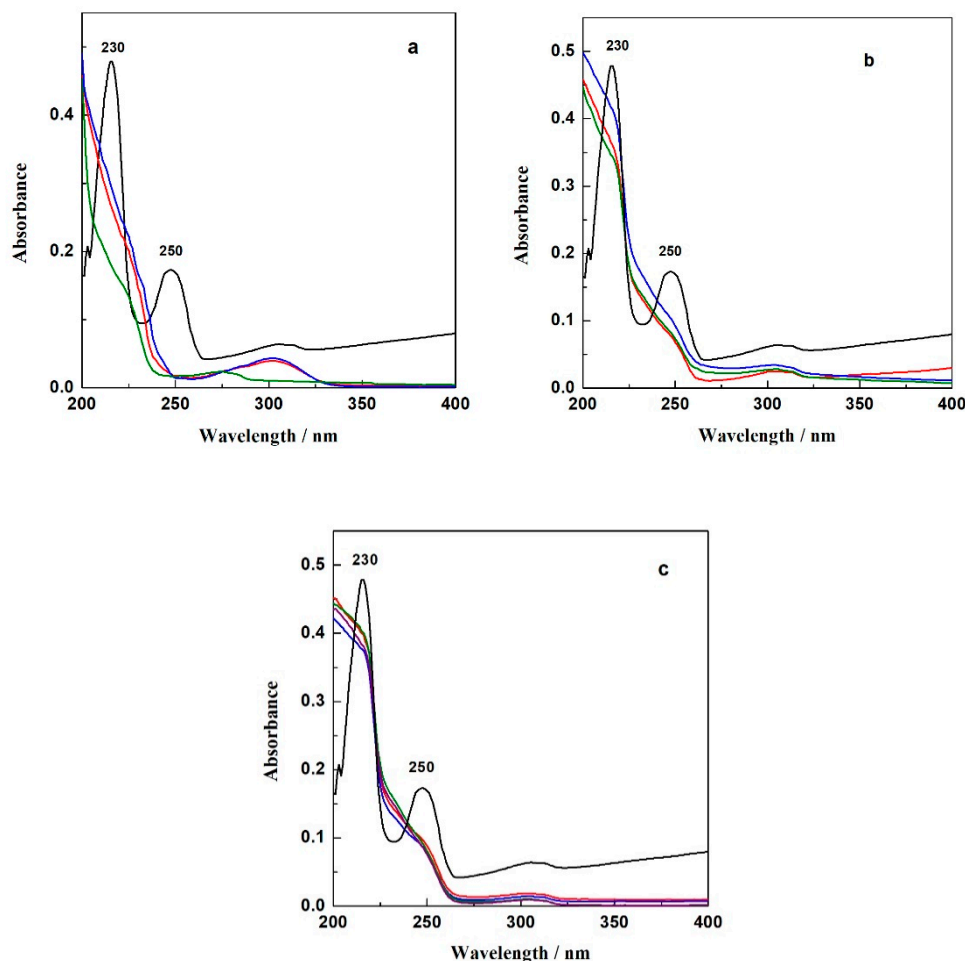


Figure 9. Changes in the UV-Vis absorption spectra of the TritonTM X-114 solution before (black curve) and (a) after 4 h of illumination with solar light in the presence of three various active layers: Fe/W/Fe (green curve), m-WFe (red curve), and W/Fe/W (blue curve); (b) in the presence of the Fe/W/Fe active layer after different solar illumination times: 2 h (blue curve), 3 h (red curve), and 4 h (green curve); (c) in the presence of the Fe/W/Fe active layer under simulated solar illumination with applied bias voltage (1.2 V) for 0.5 h (blue curve), 1 h (red curve), 1.5 h (violet curve), and 2 h (green curve).

According to the energy diagrams for both semiconductors, the electrons located in the conduction band (CB) in hematite (Fe_2O_3) can be easily transferred into the CB in tungsten oxide (WO_3), a semiconductor with a smaller band gap, thus making the charge separation more effective, and additionally contributing to the increase in the concentration of electrons in the conducting band of the WO_3 ; these are able to reduce dissolved oxygen into peroxide ($-\text{O}_2^\bullet$) or hydroxyl ($^\bullet\text{OH}$) radicals. Simultaneously, the photogenerated holes in the valence band of WO_3 can be injected into the valence band of Fe_2O_3 through heterojunction, and react with water to produce $^\bullet\text{OH}$ radicals. Lastly, the surfactants are effectively decomposed to create a simpler form by the $^\bullet\text{OH}$ radicals originating from both processes [23,52,53,65].

3. Materials and Methods

3.1. Chemicals

The following chemicals were of analytical grade quality and were utilized as received without further purification: Ultranal 68% HNO_3 (Chemman, Poland), sodium dodecylsulfate—SDS $M = 288.38 \text{ g mol}^{-1}$ (Sigma Aldrich, St. Louis, MO, USA), polyethylene glycol, polyoxyethylene-7.5-octylophenyloether (TritonTM X-114) $M = 536.0 \text{ g mol}^{-1}$ (Sigma Aldrich, St. Louis, MO, USA), sodium tungstate (Fluka), Dowex 50WX2 cation exchange resin (Fluka Analytical), iron (III) oxide (hematite, 98%, 325 μm , Alfa Aesar, Kandel, Germany), borododecatungstic acid ($\text{H}_5\text{BW}_{12}\text{O}_{40} \cdot x\text{H}_2\text{O} - \text{BW}_{12}$) (99%, City Chemical LLC, West Haven, CT, USA), and ethanol (99.8%, Aldrich, St. Louis, MO, USA), standard solutions of 1 g L^{-1} Pb (Merck). The doubly-distilled water from a Milli-Q water purification system (18 $\text{M}\Omega\text{-cm}$ resistivity) was used to prepare all solutions. Fluorine-doped tin oxide on glass substrates (FTO—10 Ohm per sheet) were purchased from Sigma Aldrich.

3.2. Preparation of the Photoactive Layer of the Semiconductors

Photoactive WO_3 films were prepared by the sol-gel method described by Santato et al. [66,67]. Briefly, a colloidal solution of tungstic acid, the precursor of mesoporous WO_3 , was prepared by introducing an aqueous solution of 0.5 mol L^{-1} Na_2WO_4 into an ion-exchange column containing proton exchange resin. During the passage of the sodium tungstic through the column, sodium cations were exchanged with protons on the stationary phase of the column, yielding tungstic acid; this was collected in a flask containing ethanol and polyethylene glycol (PEG300) as an organic structure-directing agent. A colloidal solution of the precursor of BW_{12} stabilized hematite (Fe_2O_3) particles was produced according to the following recipe, also described in our previous publication [68]. In the preparation process, a known amount (32 mg) of Fe_2O_3 particles was added to an aqueous solution of borododecatungstic acid and treated in an ultrasonic bath for 15 min in order to form a homogeneous suspension of hematite. The use of polyoxometalate (i.e., borododecatungstic acid) overlayers on the hematite surface was intended to improve the stability of the hematite in acidic conditions. In other words, the presence of borododecatungstic acid on the hematite surface protects it against corrosion or leaching of the Fe_2O_3 constituent. Moreover, photoactive materials composed of a mixture of the Keggin-type borododecatungstic acid (BW_{12}) modified hematite cluster with a tungsten oxide matrix were also produced and described (m-WFe). The hierarchical photoactive systems were created through three subsequent depositions of proper precursor solutions on pre-cleaned FTO glass substrates, employing the doctor blade technique and exposing each layer to annealing in an oven (Nabertherm-B180) with a controlled temperature (450 $^\circ\text{C}$) and in oxygen atmosphere for 30 min. To evaluate the coating thicknesses of the photoactive materials (at a 1 mm level), measurements using profilometry were performed (Talysurf 50, Rank Taylor Hobson, Middlefield, CT, USA). For comparison purposes, as well as for the determination of the best photocatalytic system for photodegradation of surfactants at various pH levels, the effects of the order of deposition of single layers were examined. The arrangements of the films utilized as photocatalytic systems in this study of surfactant photodegradation were labeled as: (1) W/Fe/W, (2) Fe/W/Fe, (3) m-WFe, and (4) 3 layers of solely WO_3 . The thicknesses of photoactive films deposited on FTO were ca. 1 μm . The ratios of tungsten to iron in the photoactive materials were determined by X-ray fluorescence (XRF) analysis (Rigaku RIX-3000, Austin, TX, USA).

3.3. Apparatus

The electrochemical measurements were carried out using a $\mu\text{Autolab}$ type II (Eco-Chemie B.V., The Netherlands) with a 663 VA Stand electrode system, using a hanging mercury drop electrode (HMDE) and Ag/AgCl (3 mol dm^{-3} KCl) as the reference electrode (Metrohm, Switzerland) for the stripping voltammetry experiments, and a CH Instruments (Austin, TX, USA) 750A workstation in a conventional three-electrode cell configuration for the photoelectrochemical experiments. All potentials

in the case of the photoelectrochemical measurements were registered versus an Hg/HgSO₄ saturated K₂SO₄ reference electrode and expressed versus the reversible hydrogen electrode (RHE) scale according to the following equation: $E_{\text{RHE}} = E_{\text{Hg/HgSO}_4}^{\text{O}} + 0.059 \cdot \text{pH} + E_{\text{experimental}}$, where E_{RHE} is the converted potential vs. RHE, $E_{\text{Hg/HgSO}_4}^{\text{O}} = 0.640$ V at 25 °C, and $E_{\text{experimental}}$ is the experimentally measured potential versus a Hg/HgSO₄ reference; a carbon rod was utilized as the counter electrode. Photocurrent density values were determined with regard to the geometric surface area of the working electrode (0.2 cm²). As a rule, photochemical measurements were conducted utilizing a Solar Light, Xe 150 W solar simulator under simulated AM 1.5 solar light irradiation, causing an illumination intensity on the photoelectrode surface of 100 mW cm⁻² (a calibrated reference cell Oriel, 91150V). The UV photodegradation processes were carried out in a stationary UV-mineralization device using an LS0308 solar lamp (LOT-QuantumDesign, Germany). All experiments were performed in a thermostated cell at a temperature of 22 ± 0.5 °C.

The photoactive systems were systematically characterized to obtain information on their morphology, homogeneity, composition, and crystal structure by various techniques, such as scanning electron microscopy (SEM), energy dispersion X-ray spectroscopy (EDS), X-ray diffraction (XRD), Raman spectroscopy, and UV-Vis spectrophotometry. The SEM experiments were performed using a Carl Zeiss Merlin instrument equipped with EDS analysis (Bruker Quantax 400, SEM-EDS, Germany). UV-Vis absorption spectra were recorded with a double beam spectrometer operating between 195 and 375 nm (UV-Vis Spectrometer, Perkin Elmer Lambda 20). The crystal structure determination and phase analysis of the proposed photoactive films were carried out by XRD using a Bruker D8 Discover system operated with a Cu-Kα1 source ($\lambda = 1.5406$ Å) and a Vantec (linear) detector ($k = 1.5406$ Å) in an angle range from 10° to 100° with a step size of 0.02° s⁻¹. The lattice parameter value and particle size were obtained from the position and the full width at half-maximum (FWHM) of the appropriate peak.

Raman spectra measurements were performed using the backscattering configuration with a LabRAM HR800 (Horiba Jobin Yvon) confocal microscope system, a Peltier-cooled CCD detector (1024 × 256 pixel), and a 150 mW He-Ne diode-pumped and frequency-doubled Nd:YAG laser (532 nm). The equipment calibration was done utilizing a silicon wafer at the 520 cm⁻¹ Raman signal. For each sample, the spectra were collected at various places on the surface in order to evaluate the uniformity of the samples, but also to provide typical characterization of the layers.

The contact angle was measured using optical tensiometer Theta Lite (Biolin Scientific, Gothenburg, Sweden). All measurements were carried out using 4 µL droplets of surfactant solutions deposited on a gold plate. These measurements were performed on three independent samples.

3.4. Photodecomposition Assisted by Semiconductors

Photodecomposition was performed in a glass tube containing 23 or 46 mL of aqueous surfactant solutions (SDS or TritonTM X-114) irradiated with a simulated AM 1.5 solar light. Initially, surfactant solutions were prepared by dissolving up to 48 µg mL⁻¹ of SDS and 11 µg mL⁻¹ of TritonTM X-114 in double-distilled water. Before irradiation, an FTO glass plate coated with the appropriate active surface layers was located in the tube containing the surfactant solution. Depending on which metal oxide was used as the top layer on the layer-by-layer systems, the surfactant solutions were adjusted to a suitable pH value of 5 (hematite on top) or 2 (WO₃ on top), using 68% nitric acid. It is noteworthy that during the irradiation of both the SDS and TritonTM X-114 solutions, no increase in the solution temperature was observed. In the case of the SDS solution, the samples were irradiated for 4 h, and for TritonTM X-114, the irradiation time was increased to 6 h, due to the fact that the nonionic surfactant is significantly more resistant to photodegradation than the anionic surfactant (i.e., SDS). As a rule, all the samples were stirred during the irradiation time, and after every hour, 10 mL of each irradiated sample were collected and stored at +4 °C until the analysis was performed. However, to increase the efficiency of the decomposition of TritonTM X-114 and SDS, a bias voltage (1.2 V vs. RHE) was applied to the samples during the irradiation (photoactive surface area of the electrode was 1 cm²). In these cases, the irradiation times were limited to 2 h, while sampling for analysis was carried out every 0.5 h.

3.5. Procedures of Pb Determination

The recovery of Pb was utilized to evaluate the degree of photodegradation of the surfactants, using differential pulse anodic stripping voltammetry (DPASV), with a mercury drop electrode (HMDE) as the working electrode. An electrode material such as mercury is especially sensitive to interference from surfactants or their oxidized byproducts. The recorded signal of any depolarizer (e.g., Pb ethyl acetate) in the presence of a surfactant is noticeably lower than recorded in the solution after decomposition or without surfactants [68]. This effect is well known and commonly accepted as an indirect tensammetric method of surfactant determination. HDME has been used for the trace analysis of Cd and Pb in wastewater [69] and uranium (U (VI)) in water [70], as well as for Cd, Cu, Pb and Zn in biological samples [71], only after UV mineralization. Therefore, an effective mineralization is required [72]. In this study, the Pb signal recorded at -0.48 V (versus the 3 mol dm^{-3} Ag/AgCl reference electrode) using differential pulse anodic stripping voltammetry (modulation time of 0.05 s and amplitude of 50 mV) was utilized as the indicator of the efficiency of surfactant photodecomposition. As a rule, the solutions were deoxygenated with argon for 15 min after every change in the sample and before the preconcentration step (75 s at -0.9 V in a stirred solution). The Pb oxidation signals were recorded at a scan rate of 10 mV s^{-1} after 5 s of resting time. The method of standard additions was employed as the voltammetric method for the quantitative determination of Pb. The supporting electrolyte was composed of DI water with HNO_3 and 1 cm^3 of the appropriate surfactant solution, as well as 20 ng of Pb (II) (as the nitrate).

4. Conclusions

Based on the results, the following conclusions are drawn: Photoactive films utilizing hierarchical and bicomponent admixtures of tungsten (VI) oxide and iron (III) oxide (hematite) have been successfully fabricated using a sol-gel method; all described photoactive materials exhibited excellent photocatalytic and photoelectrocatalytic activity towards the degradation of the anionic surfactant sodium dodecylsulfate (SDS) and the nonionic surfactant (1,1,3,3-tetramethylbutyl)phenyl-polyethylene glycol (Triton™ X-114)) under solar light irradiation. To evaluate the efficiency of decomposition of surfactants, anodic stripping voltammetry was utilized by determining the recovery of standard additions of Pb. The degradation rate of SDS and Triton™ X-114 reached 100% respectively after 2 and 3 h of solar light irradiation-assisted digestion, in the case of admixed WO_3 and Fe_2O_3 , as well as in the hierarchical system with a hematite layer between tungsten oxide layers. Moreover, the application of a bias voltage to the proposed photoactive system results in a significant enhancement in the surfactant degradation under solar light illumination (reducing the photodecomposition time to 0.5 h). The study of the water contact angle for the photodegradation product showed that they decreased with prolongation of the irradiation time, indicating effective surfactants' decomposition in the proposed photoactive systems. Furthermore, depending on whether hematite is applied as the middle layer of a "sandwich" between the WO_3 layers or as the outer layer of the photoactive films, such films can be used to decompose surfactants in acidic media of $\text{pH} < 2$ or in neutral media of $\text{pH} > 4$. It is important to note that, to the best of our knowledge, this is the first time that a binary photoactive system composed of WO_3 and Fe_2O_3 and prepared in a systematic and controlled manner has been utilized for the photodecomposition of surfactants (non-ionic and anionic) under solar light irradiation in the absence of strong oxidizing agents (e.g., H_2O_2). High photocatalytic activity towards surfactant degradation under solar light illumination can be explained in the context of a synergistic effect between both semiconductors, arising from interfacial electron transfer from WO_3 to Fe_2O_3 [65]. The utilization of hierarchized nanosemiconductor layers as the photoactive systems for reagent-free decomposition of surfactants is an alternative procedure to the methodology using digestion with the addition of hydrogen peroxide; it can be also used in the treatment of drinking water, and is a good starting point for the development of technology for solar light irradiation of contaminated reservoirs. The present results imply that designing 3D hierarchical composites with a systematic and controlled manner of the layering allows the production of more effective photocatalytic materials for the decomposition of

surfactants under solar light irradiation in water samples with different pH, whilst maintaining a high photostability of the hierarchical system.

Author Contributions: Author Contributions: B.K.-O. and K.M. conceived and designed the experiments; E.B. performed all experiments; B.K.-O. and K.M. analyzed the results; B.K.-O. and K.M. wrote the paper, and all other co-authors also participated in revising the paper.

Funding: This work was supported by the National Science Centre (Poland), project No. 2015/19/N/ST4/00915.

Acknowledgments: We acknowledge the help of Agnieszka Więckowska in performing the water contact angle measurements.

Conflicts of Interest: The authors declare no conflict of interest.

References

1. Eckert, H.; Bobeth, M.; Teixeira, S.; Kühn, K.; Cuniberti, G. Modeling of photocatalytic degradation of organic components in water by nanoparticle suspension. *Chem. Eng. J.* **2015**, *261*, 67–75. [\[CrossRef\]](#)
2. Bondi, C.A.; Marks, J.L.; Wroblewski, L.B.; Raatikainen, H.S.; Lenox, S.R.; Gebhardt, K.E. Human and Environmental Toxicity of Sodium Lauryl Sulfate (SLS): Evidence for Safe Use in Household Cleaning Products. *Environ. Health Insights* **2015**, *9*, 27–32. [\[CrossRef\]](#) [\[PubMed\]](#)
3. Yuan, C.L.; Xu, Z.Z.; Fan, M.X.; Liu, H.Y.; Xie, Y.H.; Zhu, T. Study on characteristics and harm of surfactants. *J. Chem. Pharm. Res.* **2014**, *6*, 2233–2237.
4. Chaturvedi, V.; Kumar, A. Toxicity of sodium dodecyl sulfate in fishes and animals a review. *Int. J. Appl. Biol. Pharm. Technol.* **2010**, *1*, 630–633.
5. Wang, Y.; Zhang, Y.; Li, X.; Sun, M.; Weil, Z.; Wang, Y.; Gao, A.; Chen, D.; Zhao, X.; Feng, X. Exploring the Effects of Different Types of Surfactants on Zebrafish Embryos and Larvae. *Nature* **2015**, *5*, 10107. [\[CrossRef\]](#)
6. Ospina-Alvarez, N.; Burakiewicz, P.; Sadowska, M.; Krasnodebska-Ostrega, B. TII and TIII presence in suspended particulate matter: Speciation analysis of thallium in wastewater. *Environ. Chem.* **2015**, *12*, 374–379. [\[CrossRef\]](#)
7. Gilman, L.B.; Leblanc, G.N.; Revesz, R. *Preparation of Environmental Samples for Metal Analysis Using Microwave Digestion*; CEM Corp.: Matthews, NC, USA, 1996; pp. 1–10.
8. Xue, Q.; Liu, Y.; Zhou, Q.; Utsumi, M.; Zhang, Z.; Sugiura, N. Photocatalytic degradation of geosmin by Pd nanoparticle modified WO₃ catalyst under simulated solar light. *Chem. Eng. J.* **2016**, *283*, 614–621. [\[CrossRef\]](#)
9. Robert, D.; Malato, S. Solar photocatalysis: A clean process for water detoxification. *Sci. Total Environ.* **2002**, *291*, 85–97. [\[CrossRef\]](#)
10. Golimowski, J.; Golimowska, K. UV-photooxidation as pretreatment step in inorganic analysis of environmental samples. *Anal. Chim. Acta* **1996**, *325*, 111–133. [\[CrossRef\]](#)
11. Park, H.; Park, Y.; Kim, W.; Choi, W. Surface modification of TiO₂ photocatalyst for environmental applications. *Gener. Photochem. Asia* **2013**, *15*, 1–20. [\[CrossRef\]](#)
12. Linsebigler, A.L.; Lu, G.; Yates, J.T. Photocatalysis on TiO₂ Surfaces: Principles, Mechanisms, and Selected Results. *Chem. Rev.* **1995**, *95*, 735–758. [\[CrossRef\]](#)
13. Watson, S.S.; Beydoun, D.; Scott, J.A.; Amal, R. The effect of preparation method on the photoactivity of crystalline titanium dioxide particles. *Chem. Eng. J.* **2003**, *95*, 213–220. [\[CrossRef\]](#)
14. Zhang, J.; Yan, S.; Fu, L.; Wang, F.; Yuan, M.; LUO, G.; XU, Q.; WANG, X.; LI, C. Photocatalytic Degradation of Rhodamine B on Anatase, Rutile, and Brookite TiO₂. *Chin. J. Catal.* **2011**, *32*, 983–991. [\[CrossRef\]](#)
15. Guzsvány, V.; Petrović, J.; Krstić, J.; Papp, Z.; Putek, M.; Bjelica, L.; Bobrowski, A.; Abramović, B. Renewable silver-amalgam film electrode for voltammetric monitoring of solar photodegradation of imidacloprid in the presence of Fe/TiO₂ and TiO₂ catalysts. *J. Electroanal. Chem.* **2013**, *699*, 33–39. [\[CrossRef\]](#)
16. Pelaez, M.; Nolan, N.T.; Pillai, S.C.; Seery, M.K.; Falaras, P.; Kontos, A.G.; Dunlop, P.S.M.; Hamilton, J.W.J.; Byrne, J.A.; O'Shea, K.; et al. A review on the visible light active titanium dioxide photocatalysts for environmental applications. *Appl. Catal. B Environ.* **2012**, *125*, 331–349. [\[CrossRef\]](#)
17. Bechambi, O.; Sayadi, S.; Najjar, W. Photocatalytic degradation of bisphenol A in the presence of C-doped ZnO: Effect of operational parameters and photodegradation mechanism. *J. Ind. Eng. Chem.* **2015**, *32*, 201–210. [\[CrossRef\]](#)

18. Kansal, S.K.; Singh, M.; Sud, D. Studies on photodegradation of two commercial dyes in aqueous phase using different photocatalysts. *J. Hazard. Mater.* **2007**, *141*, 581–590. [\[CrossRef\]](#)
19. Aragon, A.G.; Kierulf-Vieira, W.; Łęcki, T.; Zarębska, K.; Widera-Kalinowska, J.; Skompska, M. Synthesis and application of N-doped TiO₂/CdS/poly(1,8-diaminocarbazole) composite for photocatalytic degradation of 4-chlorophenol under visible light. *Electrochim. Acta* **2019**, *314*, 73–80. [\[CrossRef\]](#)
20. Janbandhu, S.Y.; Munishwar, S.R.; Sukhadeve, G.K.; Gedam, R.S. Effect of annealing time on optical properties of CdS QDs containing glasses and their application for degradation of methyl orange dye. *Mater. Charact.* **2019**, *152*, 230–238. [\[CrossRef\]](#)
21. Amani-Ghadim, A.R.; Khodam, F.; Seyed Dorraji, M.S. ZnS quantum dot intercalated layered double hydroxide semiconductors for solar water splitting and organic pollutant degradation. *J. Mater. Chem. A* **2019**, *7*, 11408–11422. [\[CrossRef\]](#)
22. Wang, C.-T. Photocatalytic activity of nanoparticle gold/iron oxide aerogels for azo dye degradation. *J. Non-Cryst. Solids* **2007**, *353*, 1126–1133. [\[CrossRef\]](#)
23. Bai, S.; Zhang, K.; Sun, J.; Luo, R.; Li, D.; Chen, A. Surface decoration of WO₃ architectures with Fe₂O₃ nanoparticles for visible-light-driven photocatalysis. *CrystEngComm* **2014**, *16*, 3289–3295. [\[CrossRef\]](#)
24. Sivula, K.; Le Formal, F.; Grätzel, M. Solar Water Splitting: Progress Using Hematite (α -Fe₂O₃) Photoelectrodes. *ChemSusChem* **2011**, *4*, 432–449. [\[CrossRef\]](#) [\[PubMed\]](#)
25. Luo, J.; Steier, L.; Son, M.-K.; Schreier, M.; Mayer, M.T.; Grätzel, M. Cu₂O Nanowire Photocathodes for Efficient and Durable Solar Water Splitting. *Nano Lett.* **2016**, *16*, 1848–1857. [\[CrossRef\]](#) [\[PubMed\]](#)
26. Pouretedal, H.R.; Tofangsazi, Z.; Keshavarz, M.H. Photocatalytic activity of mixture of ZrO₂/SnO₂, ZrO₂/CeO₂ and SnO₂/CeO₂ nanoparticles. *J. Alloys Compd.* **2012**, *513*, 359–364. [\[CrossRef\]](#)
27. Sayama, K.; Hayashi, H.; Arai, T.; Yanagida, M.; Gunji, T.; Sugihara, H. Highly active WO₃ semiconductor photocatalyst prepared from amorphous peroxo-tungstic acid for the degradation of various organic compounds. *Appl. Catal. B Environ.* **2010**, *94*, 150–157. [\[CrossRef\]](#)
28. Krasnodębska-Ostrega, B.; Bielecka, A.; Biaduń, E.; Miecznikowski, K. Mesoporous film of WO₃—the “sunlight” assisted decomposition of surfactant in wastewater for voltammetric determination of Pb. *Appl. Surf. Sci.* **2016**, *388*, 746–752. [\[CrossRef\]](#)
29. Karunakaran, C.; Senthilvelan, S. Vanadia-catalyzed solar photooxidation of aniline. *J. Colloid Interface Sci.* **2005**, *289*, 466–471. [\[CrossRef\]](#)
30. Thirugnanam, N.; Song, H.; Wu, Y. Photocatalytic degradation of Brilliant Green dye using CdSe quantum dots hybridized with graphene oxide under sunlight irradiation. *Chin. J. Catal.* **2017**, *38*, 2150–2159. [\[CrossRef\]](#)
31. He, G.-H.; He, G.-L.; Li, A.-J.; Li, X.; Wang, X.-J.; Fang, Y.-P.; Xu, Y.-H. Synthesis and visible light photocatalytic behavior of WO₃ (core)/Bi₂WO₆ (shell). *J. Mol. Catal. Chem.* **2014**, *385*, 106–111. [\[CrossRef\]](#)
32. Bamwenda, G.R.; Arakawa, H. The visible light induced photocatalytic activity of tungsten trioxide powders. *Appl. Catal. Gen.* **2001**, *210*, 181–191. [\[CrossRef\]](#)
33. Martínez-de la Cruz, A.; Martínez, D.S.; Cuéllar, E.L. Synthesis and characterization of WO₃ nanoparticles prepared by the precipitation method: Evaluation of photocatalytic activity under vis-irradiation. *Solid State Sci.* **2010**, *12*, 88–94. [\[CrossRef\]](#)
34. Vamvasakis, I.; Georgaki, I.; Vernardou, D.; Kenanakis, G.; Katsarakis, N. Synthesis of WO₃ catalytic powders: Evaluation of photocatalytic activity under NUV/visible light irradiation and alkaline reaction pH. *J. Sol-Gel Sci. Technol.* **2015**, *76*, 120–128. [\[CrossRef\]](#)
35. Wang, C.; Huang, Z. Controlled synthesis of α -Fe₂O₃ nanostructures for efficient photocatalysis. *Mater. Lett.* **2016**, *164*, 194–197. [\[CrossRef\]](#)
36. Davi, M.; Ogutu, G.; Schrader, F.; Rokicinska, A.; Kustrowski, P.; Slabon, A. Enhancing Photoelectrochemical Water Oxidation Efficiency of WO₃/ α -Fe₂O₃ Heterojunction Photoanodes by Surface Functionalization with CoPd Nanocrystals. *Eur. J. Inorg. Chem.* **2017**, *2017*, 4267–4274. [\[CrossRef\]](#)
37. Li, Y.; Feng, J.; Li, H.; Wei, X.; Wang, R.; Zhou, A. Photoelectrochemical splitting of natural seawater with α -Fe₂O₃/WO₃ nanorod arrays. *Int. J. Hydrogen Energy* **2016**, *41*, 4096–4105. [\[CrossRef\]](#)
38. Sivula, K.; Formal, F.L.; Grätzel, M. WO₃–Fe₂O₃ Photoanodes for Water Splitting: A Host Scaffold, Guest Absorber Approach. *Chem. Mater.* **2009**, *21*, 2862–2867. [\[CrossRef\]](#)
39. Mao, A.; Kim, J.K.; Shin, K.; Wang, D.H.; Yoo, P.J.; Han, G.Y.; Park, J.H. Hematite modified tungsten trioxide nanoparticle photoanode for solar water oxidation. *J. Power Sources* **2012**, *210*, 32–37. [\[CrossRef\]](#)

40. Li, Y.; Zhang, L.; Liu, R.; Cao, Z.; Sun, X.; Liu, X.; Luo, J. WO₃@ α -Fe₂O₃ Heterojunction Arrays with Improved Photoelectrochemical Behavior for Neutral pH Water Splitting. *ChemCatChem* **2016**, *8*, 2765–2770. [\[CrossRef\]](#)
41. Macías-Tamez, R.; Villanueva-Rodríguez, M.; Ramos-Delgado, N.A.; Maya-Treviño, L.; Hernández-Ramírez, A. Comparative Study of the Photocatalytic Degradation of the Herbicide 2,4-D Using WO₃/TiO₂ and Fe₂O₃/TiO₂ as Catalysts. *Water Air Soil Pollut.* **2017**, *228*, 379. [\[CrossRef\]](#)
42. Wang, H.; Wang, C.; Cui, X.; Qin, L.; Ding, R.; Wang, L.; Liu, Z.; Zheng, Z.; Lv, B. Design and facile one-step synthesis of FeWO₄/Fe₂O₃ di-modified WO₃ with super high photocatalytic activity toward degradation of quasi-phenothiazine dyes. *Appl. Catal. B Environ.* **2018**, *221*, 169–178. [\[CrossRef\]](#)
43. Memar, A.; Daud, W.R.W.; Hosseini, S.; Eftekhari, E.; Minggu, L.J. Study on photocurrent of bilayers photoanodes using different combination of WO₃ and Fe₂O₃. *Sol. Energy* **2010**, *84*, 1538–1544. [\[CrossRef\]](#)
44. Memar, A.; Phan, C.M.; Tade, M.O. Photocatalytic activity of WO₃/Fe₂O₃ nanocomposite photoanode. *Int. J. Hydrogen Energy* **2015**, *40*, 8642–8649. [\[CrossRef\]](#)
45. Müller, A.; Kondofersky, I.; Folger, A.; Fattakhova-Rohlfing, D.; Bein, T.; Scheu, C. Dual absorber Fe₂O₃/WO₃ host-guest architectures for improved charge generation and transfer in photoelectrochemical applications. *Mater. Res. Express* **2017**, *4*, 016409. [\[CrossRef\]](#)
46. Hosseini, S.; Eftekhari, E.; Masoudi Soltani, S.; Memar, A.; Eghbali Babadi, F.; Dastorian Jamnani, B.; Ismail, M.H.S.; Jeffery Minggu, L. Effect of intermediate layer in photocurrent improvement of three-layer photoanodes using WO₃ and Fe₂O₃. *J. Environ. Chem. Eng.* **2013**, *1*, 1309–1314. [\[CrossRef\]](#)
47. Kronawitter, C.X.; Vayssieres, L.; Shen, S.; Guo, L.; Wheeler, D.A.; Zhang, J.Z.; Antoun, B.R.; Mao, S.S. A perspective on solar-driven water splitting with all-oxide hetero-nanostructures. *Energy Environ. Sci.* **2011**, *4*, 3889–3899. [\[CrossRef\]](#)
48. Jin, T.; Diao, P.; Wu, Q.; Xu, D.; Hu, D.; Xie, Y.; Zhang, M. WO₃ nanoneedles/ α -Fe₂O₃/cobalt phosphate composite photoanode for efficient photoelectrochemical water splitting. *Appl. Catal. B Environ.* **2014**, *148–149*, 304–310. [\[CrossRef\]](#)
49. Hosseini, S.; Eftekhari, E.; Soltani, S.M.; Babadi, F.E.; Minggu, L.J.; Ismail, M.H.S. Synthesis, characterization and performance evaluation of three-layered photoanodes by introducing a blend of WO₃ and Fe₂O₃ for dye degradation. *Appl. Surf. Sci.* **2014**, *289*, 53–61. [\[CrossRef\]](#)
50. Senthil, R.A.; Priya, A.; Theerthagiri, J.; Selvi, A.; Nithyadharseni, P.; Madhavan, J. Facile synthesis of α -Fe₂O₃/WO₃ composite with an enhanced photocatalytic and photo-electrochemical performance. *Ionics* **2018**, *24*, 3673–3684. [\[CrossRef\]](#)
51. Lei, R.; Ni, H.; Chen, R.; Zhang, B.; Zhan, W.; Li, Y. Hydrothermal synthesis of WO₃/Fe₂O₃ nanosheet arrays on iron foil for photocatalytic degradation of methylene blue. *J. Mater. Sci. Mater. Electron.* **2017**, *28*, 10481–10487. [\[CrossRef\]](#)
52. Barreca, D.; Carraro, G.; Gasparotto, A.; Maccato, C.; Sada, C.; Bontempi, E.; Brisotto, M.; Pliekhova, O.; Štancar, U.L. Novel two-step vapor-phase synthesis of UV–Vis light active Fe₂O₃/WO₃ nanocomposites for phenol degradation. *Environ. Sci. Pollut. Res.* **2016**, *23*, 20350–20359. [\[CrossRef\]](#)
53. Bi, D.; Xu, Y. Improved Photocatalytic Activity of WO₃ through Clustered Fe₂O₃ for Organic Degradation in the Presence of H₂O₂. *Langmuir* **2011**, *27*, 9359–9366. [\[CrossRef\]](#)
54. Priyadharsan, A.; Vasanthakumar, V.; Shanavas, S.; Karthikeyan, S.; Anbarasan, P.M. Crumpled sheet like graphene based WO₃-Fe₂O₃ nanocomposites for enhanced charge transfer and solar photocatalysts for environmental remediation. *Appl. Surf. Sci.* **2019**, *470*, 114–128. [\[CrossRef\]](#)
55. Azimirad, R.; Akhavan, O.; Moshfegh, A.Z. The effect of heat treatment on physical properties of nanograined (WO₃)_{1-x}-(Fe₂O₃)_x thin films. *Vacuum* **2011**, *85*, 810–819. [\[CrossRef\]](#)
56. Miecznikowski, K.; Ramírez, A.; Fiechter, S.; Bogdanoff, P.; Szaniawska, E.; Wadas, A.; Kulesza, P.J. Development of Hybrid Tungsten Oxide Photoanodes Admixed with Borododecatungstate-Polyanion Modified-Hematite: Enhancement of Water Oxidation upon Irradiation with Visible Light. *Ubiquitous Electrochem.* **2015**, *179*, 379–385. [\[CrossRef\]](#)
57. Barczuk, P.J.; Krolikowska, A.; Lewera, A.; Miecznikowski, K.; Solarska, R.; Augustynski, J. Structural and photoelectrochemical investigation of boron-modified nanostructured tungsten trioxide films. *Electrochim. Acta* **2013**, *104*, 282–288. [\[CrossRef\]](#)
58. Solarska, R.; Bieńkowski, K.; Królikowska, A.; Dolata, M.; Augustyński, J. Nanoporous WO₃-Fe₂O₃ films; structural and photo-electrochemical characterization. *Funct. Mater. Lett.* **2014**, *07*, 1440006. [\[CrossRef\]](#)

59. Cao, J.; Luo, B.; Lin, H.; Xu, B.; Chen, S. Thermodecomposition synthesis of $\text{WO}_3/\text{H}_2\text{WO}_4$ heterostructures with enhanced visible light photocatalytic properties. *Appl. Catal. B Environ.* **2012**, *111–112*, 288–296. [CrossRef]
60. Yang, C.; Sang, Q.; Zhang, S.; Huang, W. Voltammetric determination of estrone based on the enhancement effect of surfactant and a MWNT film electrode. *Mater. Sci. Eng. C* **2009**, *29*, 1741–1745. [CrossRef]
61. Biaduń, E.; Nowak, N.; Kowalska, J.; Miecznikowski, K.; Krasnodebska-Ostrega, B. Organic matter decomposition before arsenic speciation analysis of water sample—“Soft decomposition” using nano-photocatalysts. *Chemosphere* **2018**, *207*, 481–488. [CrossRef]
62. Aonyas, M.M.; Nešić, J.; Jović, M.; Marković, M.; Dojčinović, B.; Obradović, B.; Roglić, G.M. Degradation of Triton X-100 in Water Falling Film Dielectric Barrier Discharge Reactor. *CLEAN Soil Air Water* **2016**, *44*, 422–429. [CrossRef]
63. Zhang, Y. Heterogeneous Photocatalytic Degradation of Triton X-100 in Aqueous TiO_2 Suspensions. *Am. J. Environ. Prot.* **2014**, *3*, 28. [CrossRef]
64. Saïen, J.; Ojaghloo, Z.; Soleymani, A.R.; Rasoulifard, M.H. Homogeneous and heterogeneous AOPs for rapid degradation of Triton X-100 in aqueous media via UV light, nano titania hydrogen peroxide and potassium persulfate. *Chem. Eng. J.* **2011**, *167*, 172–182. [CrossRef]
65. Bi, D.; Xu, Y. Synergism between Fe_2O_3 and WO_3 particles: Photocatalytic activity enhancement and reaction mechanism. *J. Mol. Catal. Chem.* **2013**, *367*, 103–107. [CrossRef]
66. Santato, C.; Odziemkowski, M.; Ulmann, M.; Augustynski, J. Crystallographically Oriented Mesoporous WO_3 Films: Synthesis, Characterization, and Applications. *J. Am. Chem. Soc.* **2001**, *123*, 10639–10649. [CrossRef]
67. Santato, C.; Ulmann, M.; Augustynski, J. Enhanced Visible Light Conversion Efficiency Using Nanocrystalline WO_3 Films. *Adv. Mater.* **2001**, *13*, 511–514. [CrossRef]
68. Szymanski, A.; Wyrwas, B.; Lukaszewski, Z. Determination of non-ionic surfactants and their biotransformation by-products adsorbed on alive activated sludge. *Water Res.* **2003**, *37*, 281–288. [CrossRef]
69. Lejbt, B.; Ospina-Alvarez, N.; Miecznikowski, K.; Krasnodebska-Ostrega, B. TiO_2 assisted photo-oxidation of wastewater prior to voltammetric determination of trace metals: Eco-friendly alternative to traditional digestion methods. *Appl. Surf. Sci.* **2016**, *388*, 664–669. [CrossRef]
70. Woldemichael, G.; Tulu, T.; Flechsig, G.-U. Solar UV-assisted sample preparation of river water for ultra-trace determination of uranium by adsorptive stripping voltammetry. *Microchim. Acta* **2012**, *179*, 99–104. [CrossRef]
71. do Nascimento, P.C.; da S. Marques, M.; Hilgemann, M.; de Carvalho, L.M.; Bohrer, D.; Pomblum, S.G.; Schirmer, S. Simultaneous Determination of Cadmium, Copper, Lead and Zinc in Amino Acid Parenteral Nutrition Solutions by Anodic Stripping Voltammetry and Sample Digestion by UV Irradiation. *Anal. Lett.* **2006**, *39*, 777–790.
72. Stryjewska, E.; Krasnodebska, B.; Biała, H.; Rubel, J.T.S. Heavy Metal Determination in Moss Samples from the Kampinos National Park. *Chem. Anal. Wars.* **1996**, *39*, 483–491.



© 2019 by the authors. Licensee MDPI, Basel, Switzerland. This article is an open access article distributed under the terms and conditions of the Creative Commons Attribution (CC BY) license (<http://creativecommons.org/licenses/by/4.0/>).